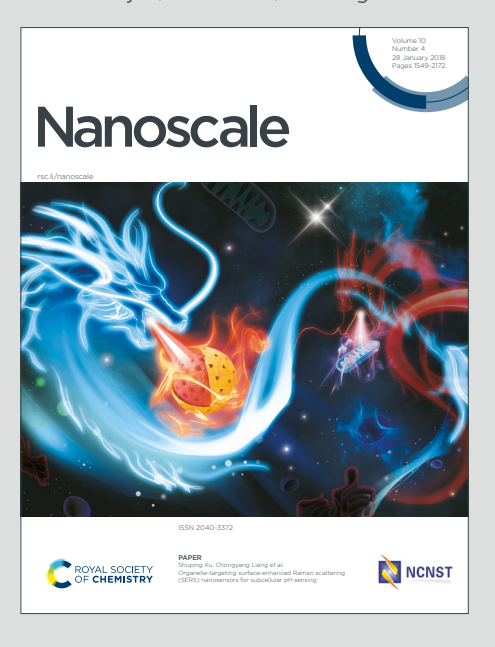




Nanoscale

Accepted Manuscript

This article can be cited before page numbers have been issued, to do this please use: B. Gaykwad, S. H. Bharadwaj H, A. Bahirat, R. Ranganathan and K. Jasuja, *Nanoscale*, 2025, DOI: 10.1039/D5NR01185J.



This is an Accepted Manuscript, which has been through the Royal Society of Chemistry peer review process and has been accepted for publication.

Accepted Manuscripts are published online shortly after acceptance, before technical editing, formatting and proof reading. Using this free service, authors can make their results available to the community, in citable form, before we publish the edited article. We will replace this Accepted Manuscript with the edited and formatted Advance Article as soon as it is available.

You can find more information about Accepted Manuscripts in the <u>Information for Authors</u>.

Please note that technical editing may introduce minor changes to the text and/or graphics, which may alter content. The journal's standard <u>Terms & Conditions</u> and the <u>Ethical guidelines</u> still apply. In no event shall the Royal Society of Chemistry be held responsible for any errors or omissions in this Accepted Manuscript or any consequences arising from the use of any information it contains.



Bhagyashri Gaykwad^a, Sree Harsha Bharadwaj H^{§b} Archit Bahirat^{§b}, Raghavan Ranganathan^b, and Kabeer Jasuja^a*

- ^a Department of Chemical Engineering, Indian Institute of Technology Gandhinagar, Palaj, Gandhinagar, Gujarat 382055, India
- ^b Department of Materials Engineering, Indian Institute of Technology Gandhinagar, Palaj, Gandhinagar, Gujarat 382055, India
- *Corresponding author: kabeer@iitgn.ac.in
- § S.H.B and A.B. contributed equally to this work

Abstract:

This article is licensed under a Creative Commons Attribution 3.0 Unported Licence

Open Access Article. Published on 21 May 2025. Downloaded on 6/5/2025 2:17:29 PM.

AlB₂-type metal diborides have garnered significant attention in recent years owing to their ability to yield quasi-2D nanostructures. Titanium diboride (TiB₂), a key member of the metal diboride family, is well known for its extraordinary mechanical properties. However, the candidacy of TiB₂-based nanosheets to reinforce a polymer matrix has largely remained unexplored. In this work, we compare three kinds of TiB₂ reinforcements – bulk form, pristine nanosheets, and functionalized nanosheets, for their prospects in the mechanical reinforcement of polyurethane (PU). We find that while all fillers lead to an improvement in the mechanical properties of PU, the composite comprising pristine nanosheets exhibits the most significant enhancement. A 2 wt.% loading of pristine nanosheets results in ~80% increase in ultimate tensile strength and toughness. Detailed molecular dynamics simulations reveal that the TiB₂ nanosheets are not only able to distribute load effectively, but they also promote isotropic mechanical behaviour, which makes the composite stiff and strong. These insights are supplemented by inferences from the hydrogen bonding index (HBI) and degree of phase separation (DPS). This study exemplifies the rich prospects offered by the metal diboride-derived nanosheets for reinforcing polymer matrices.

Keywords:

XBenes, two-dimensional (2D) materials, titanium diboride, polyurethane nanocomposite, mechanical properties, simulation, tensile strength

Open Access Article. Published on 21 May 2025. Downloaded on 6/5/2025 2:17:29 PM.

This article is licensed under a Creative Commons Attribution 3.0 Unported Licence.

Introduction: View Article Online DOI: 10.1039/D5NR01185J

Since the discovery of graphene in 2004, a broad spectrum of two-dimensional (2D) materials has evolved from van der Waals (vdW) layered materials. 1-4 The extraordinary intrinsic properties offered by these 2D materials have led to a number of new advances in science and technology.⁵ Researchers have utilized these 2D materials in the form of standalone entities⁶⁻⁸ as well as in the form of fillers within nanocomposites.^{9,10} Several novel nanocomposites with unprecedented properties have been made possible by virtue of 2D materials and their rich diversity. 11-14 One such frontier that has garnered significant attention is wherein 2D materials are integrated within the polymer matrices to reinforce their mechanical properties. 15-17 For example, the tensile strength of polyurethane (PU) can be increased by ~239% upon the addition of graphene (2 % by wt.)¹⁸ and by ~80% upon addition of boron nitride nanosheets (2 % by wt.).19 Similarly, the tensile strength of nylon-6 can be improved by ~80% by adding a small fraction of functionalized molybdenum disulfide nanosheets (≤1% by wt.).20 Such extraordinary enhancements, even with a minuscule amount of nanofillers, have been attributed to the intrinsic mechanical strength of 2D materials, their high surface-to-volume ratio that enables an active interaction with the polymer matrix, and the ability of such interfaces to effectively distribute stress. 18-20

Recent years have witnessed another important advance in the science of 2D materials which is that strongly bonded non-van der Waals (non-vdW) layered materials can also be exfoliated into their quasi-2D counterparts. The availability of such quasi-2D nanostructures has created opportunities to create robust interfaces which were otherwise not possible. This is exemplified by MXenes-based polymeric nanocomposites, where nanosheets derived from MAX phase precursors have been interfaced with several polymers. ²¹ The addition of MXenes has also been found to significantly enhance the mechanical properties of polymers. For instance, the tensile strength of PU increased by 47.1 % after adding just 0.5 wt.% MXenes. ²² Similarly, an addition of 6.7 vol.% of MXenes improved the Young's modulus of poly (vinylidene fluoride) by 67 %. ²³ Such extraordinary enhancements indicate the rich prospect that quasi-2D materials derived from non-vdW layered materials offer in reinforcing the mechanical properties of polymer matrices.

AlB₂-type metal diborides represent one such family of non-vdW materials that has received renewed interest from the scientific community on account of their feasibility to be exfoliated into nanosheets. Such quasi-2D counterparts derived from AlB₂-type metal diborides have recently been named *XBenes*.²⁴ During the last decade, researchers have been

Open Access Article. Published on 21 May 2025. Downloaded on 6/5/2025 2:17:29 PM.

able to exfoliate several members of this family, including MgB₂,^{25–27} AlB₂,²⁷ TaB₂(10.1039) McRo11853 TiB₂^{28,30–32} into their quasi-2D counterparts. These nanosheets present a rich prospect as nano additives for mechanical reinforcement owing to the extraordinary mechanical properties of bulk metal diborides.^{33,34} Specifically, nanosheets derived from titanium diboride (TiB₂) could be potentially useful for reinforcing polymer matrices. This is because of the fact that TiB₂ itself is known for its extraordinary mechanical properties – the elastic modulus of bulk TiB₂ is ~565 GPa, which is about thirty times more than that of graphite (15-20 MPa) and seventy times more than MAX phases (2-8 MPa).^{34–36} Researchers have reported that the addition of bulk TiB₂ is a promising way to enhance the stiffness of metal-matrix composites.^{37–39} However, to date, there are no reports that have systematically studied the effect of nanosheets of TiB₂ as a reinforcement on the mechanical properties of polymers.

The ability to exfoliate TiB₂ in a processable dispersion has opened new avenues for the fabrication of polymer composites. Till now, researchers have reported several synthesis routes to obtain nanosheets from bulk TiB₂. In 2019, Anappara and co-workers reported the synthesis of hydroxyl-functionalized nanosheets *via* shear mixing and sonication of TiB₂.⁴⁰ Subsequently, in 2020, our group reported a peroxo-based non-classical dissolution and recrystallization route to synthesize oxy-functionalized nanosheets from TiB₂.³² In 2020, we developed a co-solvent approach to obtain minimally functionalized nanosheets of TiB₂, where an optimal ratio of isopropanol (IPA) and water was utilized for exfoliation.⁴¹ In 2021, Green and co-workers obtained nearly pristine nanosheets of TiB₂ by using ultrasonication in an organic solvent.²⁸ Recently, our group has reported the synthesis of pristine nanosheets of TiB₂ using surfactant-assisted exfoliation³¹ and ball mill-assisted mechanical exfoliation.³⁰ The availability of such a diverse pool of TiB₂ nanosheets presents an opportunity to systematically understand the effect of interfacing quasi-2D forms of TiB₂ with the polymer.

In this study, we investigate three different kinds of TiB₂-based fillers for mechanical reinforcement of base polymer– *bulk* TiB₂ particles (b-TiB₂), *pristine nanosheets* exfoliated from TiB₂(p-NS), and *functionalized nanosheets* derived from TiB₂(f-NS). We chose ball mill-assisted mechanical exfoliation³⁰ for synthesizing p-NS and dissolution-recrystallization³² for synthesizing f-NS. The p-NS fillers are selected due to their retained lattice crystal structure, which remains nearly identical to the parent material, enabling direct comparison with b-TiB₂. In contrast, f-NS are crucial for investigating the combined effects of nano scaling and functional groups compared with b-TiB₂.

To investigate the effect of TiB_2 -based nanosheets on the mechanical properties $Vioi f_{Adjicle}^{Adjicle}$ on the mechanical p

Among all the fillers, we find that the quasi-planar nature of p-NS combined with the retained chemical integrity leads to the effective reinforcement in PU matrix. In contrast, the presence of hydrophilic functional groups and distorted crystal lattices in f-NS limits their ability to reinforce the PU matrix. We show how the native metal boride lattice is seminal to the reinforcing ability of TiB₂ nano additives. We also conducted molecular dynamics (MD) simulations of PU and its composites (incorporating TiB₂ nanosheets) and obtained insights that supplement these findings. In the following sections, we elucidate how these nanofillers interface with the PU matrix and result in reinforcement.

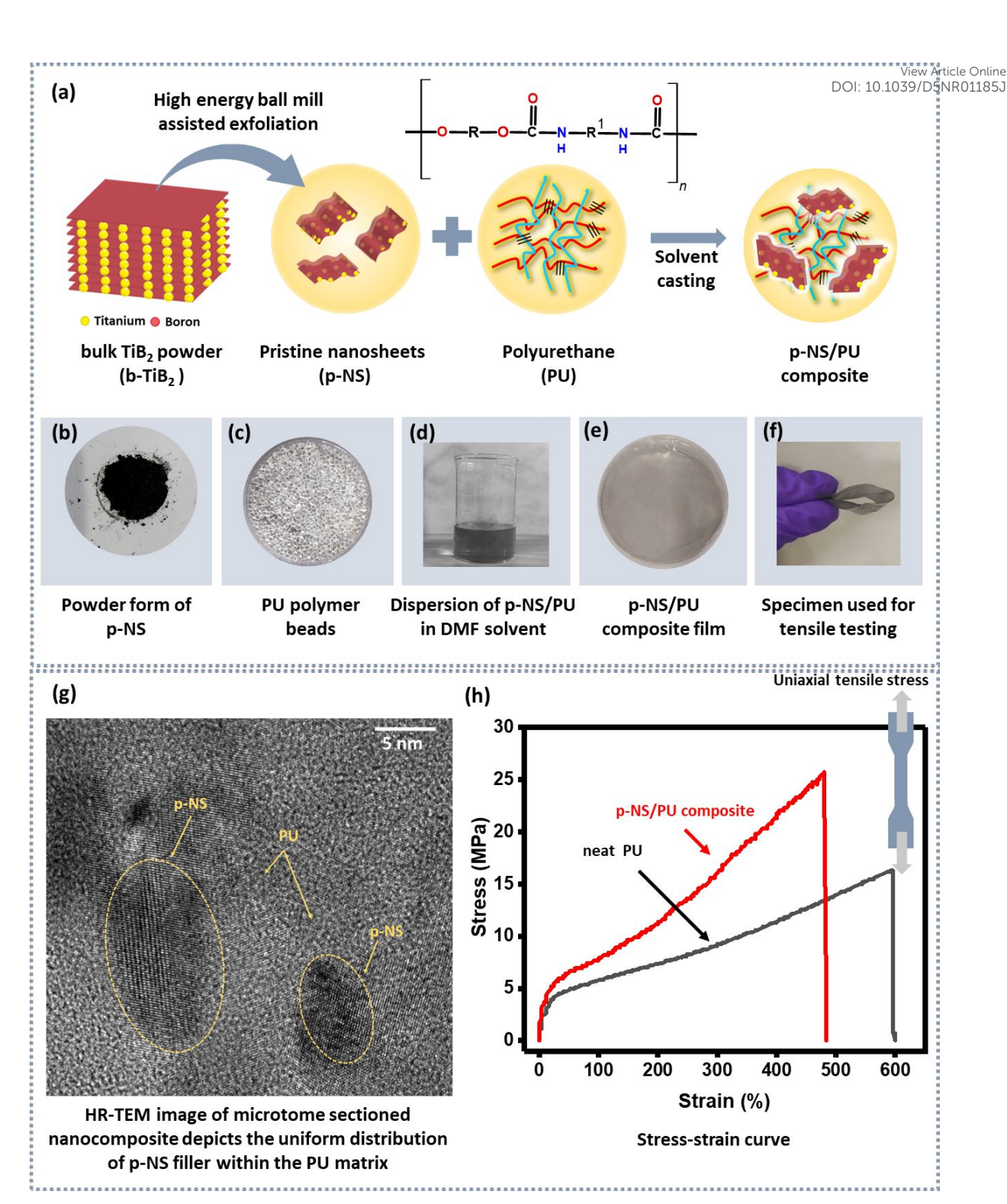


Figure 1. Graphical representation of preparing TiB₂ nanosheet -based composites using solvent casting approach. (a) Synthesis of pristine nanosheets (p-NS) using high energy ball mill-assisted mechanical exfoliation and preparation of p-NS/PU composite film. (b) Powder form of p-NS, (c) Polyurethane beads (PU), (d) Dispersion of p-NS/PU in DMF solvent, (e) Prepared composite film, (f) Demonstration of the specimen used for tensile testing, (g) HR-TEM image of microtome sectioned portion of p-NS/PU composite exhibits well-dispersed

nanosheets within PU matrix. (h) The stress-strain curve of neat PU film and $p_{\overline{0}}N_{\overline{0}}$ projecte online composite indicates that the addition of p-NS significantly enhances the native mechanical properties of the PU.

Results and Discussion:

To investigate the effect of TiB₂-based nanosheets on the mechanical properties of a polymeric system, we choose polyurethane (PU) as the polymer matrix. We prepared three type of TiB₂/PU composites by using the bulk form of TiB₂ and nanosheets derived from TiB₂ (p-NS and f-NS). We name these three types of composites b-TiB₂/PU, p-NS/PU, and f-NS/PU, respectively. For each of these composites, we prepared five variants by adding the fillers at 0.5, 1, 1.5, 2, and 5 wt.% and compared their mechanical performance with neat PU film.

We first present the structural and chemical features of these TiB₂ fillers briefly (for a detailed explanation, refer to ref. 30 and ref. 32). Figure 2a presents an FE-SEM micrograph of b-TiB₂ indicating thick crystals with micron-scale lateral dimensions as expected. TEM image also supports this observation (Figure 2d). Figure 2b illustrates the FE-SEM micrograph of p-NS synthesized using ball mill-assisted mechanical exfoliation (as reported recently by our group).³⁰ This FE-SEM image depicts planar morphology with lateral sizes in the 100-300 nm range with an aspect ratio of 25. TEM image (Figure 2e) and AFM images of p-NS (Figure S1a-b in Electronic Supplementary Information (ESI)) validate the quasi-2D nature of these nanostructures. Figure 2c shows the FE-SEM micrograph of f-NS synthesized using dissolution and non-classical recrystallization, as reported by our group earlier.³² This micrograph indicates >1 μm lateral size with crumpled morphology. TEM image (Figure 2f) and AFM images (Figure S1(c, d)) also confirmed their quasi-2D nature.

Open Access Article. Published on 21 May 2025. Downloaded on 6/5/2025 2:17:29 PM.

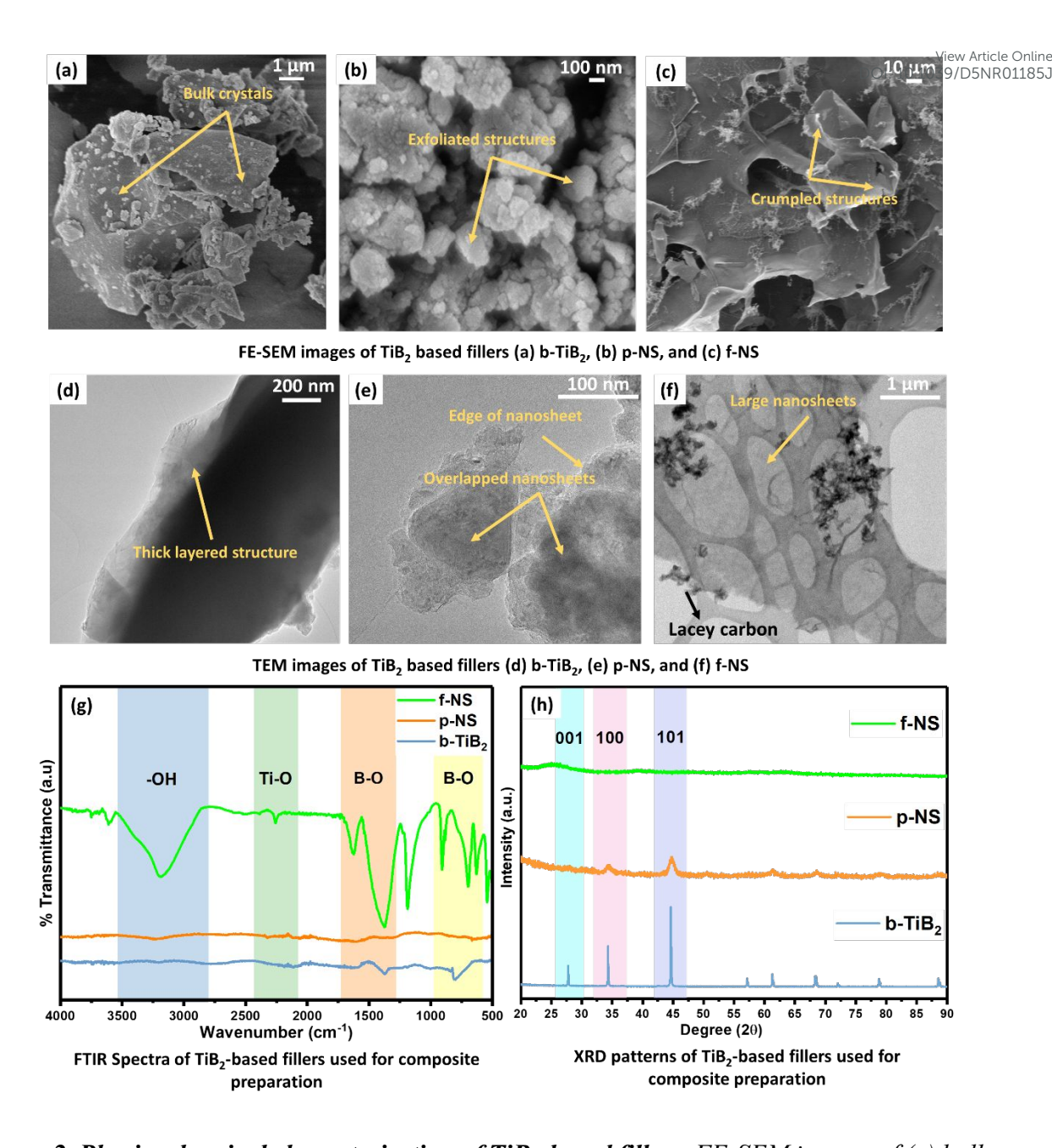


Figure 2. Physicochemical characterization of TiB_2 -based fillers. FE-SEM images of (a) bulk TiB_2 (b- TiB_2), (b) pristine nanosheets (p-NS), (c) functionalized nanosheets (f-NS) obtained using the powder form of nanosheets depict substantial differences in the lateral size of nanosheets because of different synthesis methods. TEM images of (d) b- TiB_2 , (e) p-NS, (f) f-NS obtained by drop-casting the dispersion of these nanosheets on lacey carbon grids, which depict the planar nature of such nanosheets, (g) FTIR spectra of TiB_2 based fillers – b- TiB_2 and p-NS fillers, exhibit featureless spectra, and f-NS indicate the extensive presence of oxyfunctional groups, (h) XRD patterns of b- TiB_2 and its nano scaled counterparts displaying the

Open Access Article. Published on 21 May 2025. Downloaded on 6/5/2025 2:17:29 PM.

varying range of intensities. The reduction in intensity signifies that exfoliation in intensity significant exposure in the intensity of the intensity significant exposure in the intensity of the intensity significant exposure in the intensity of the int

To ascertain the degree of functionalization in these TiB₂-based fillers, we recorded FTIR spectra. As shown in Figure 2g, b-TiB₂ and p-NS exhibit almost featureless spectra, indicating minimal functionalization as expected. The FTIR spectra of f-NS indicate heavy chemical functionalization with Ti-O, B-O, and -OH functional groups. This aligns with the observation on functionalization endowed by the chemical synthesis route.³² We performed an XRD analysis on these fillers to obtain further insights. Figure 2h presents XRD patterns of b-TiB₂, p-NS, and f-NS. The b-TiB₂ powder exhibits sharp peaks at 2θ values of 27.78°, 34.21°, and 44.71°, which correspond to the (001), (100), and (101) crystal planes, respectively. These peaks are in good agreement with the standard TiB₂ database (ICDD card no. 00-035-0741). XRD pattern of p-NS also exhibits these peaks albeit with reduced intensities – this suggests that the crystallinity of TiB₂ has been retained to a large extent during exfoliation. Specifically, the reduced intensity of peak corresponding to the (001) plane in the p-NS XRD pattern indicates a decrease in the number of Ti and B-layers in the c-direction. The reduced intensities of peaks corresponding to other planes are attributed to the randomness introduced in the crystal structure during exfoliation. The XRD pattern of f-NS did not exhibit any diffraction peaks, which is in line with the heavy chemical functionalization indicating their amorphous nature.

We prepared the composites of PU with TiB₂-based fillers using solvent casting approach (refer to methods for a detailed procedure). To understand how the TiB₂-based fillers are distributed within the polymer matrix, we examined the morphologies of composite films using FE-SEM and TEM. We depict FE-SEM images of neat PU, b-TiB₂/PU, p-NS/PU, and f-NS/PU composites at 2 wt.% loading. While neat PU exhibits a smooth surface with subtle spherulitic domains, PU composites comprising TiB₂-based fillers exhibit uneven surfaces with prominent spherulitic domains (Figure S2, ESI). Such spherulites are known to form in thermoplastics when a polymer solidifies from its melt solution.⁵⁰ TiB₂-based fillers are likely acting as heterogeneous nucleating agents, promoting more prominent domains. Zhang et al.⁵¹ made a similar observation wherein MXenes induced heterogeneous nucleation and were centred at spherulitic domains. While these results indicate that there is a change in crystallinity upon adding TiB2-based fillers, the DSC results indicate that the crystallinity of all the composites remains low (as explained in the section on physico-chemical insights). We also carried out HR-TEM imaging of a microtome section obtained from one of the nanocomposite

Open Access Article. Published on 21 May 2025. Downloaded on 6/5/2025 2:17:29 PM.

films to assess if the TiB₂ nanosheets are well distributed within the PU matrix_{0.1}Thresticle Online microtome-sectioned HR-TEM images depict that p-NS are indeed distributed within PU in a uniform manner (Figure S3, ESI). This is also reflected in the dynamic mechanical response of TiB₂-based composite (as explained in Figure S4, ESI). We have also shown the XPS survey scan of neat PU and p-NS/PU composite in Figure S5-S7.

To understand how TiB₂-based fillers affect the mechanical properties of PU, we performed uniaxial tensile testing of composites at different weight fractions – 0, 0.5, 1, 1.5, 2, and 5%. We tested at least three samples for each weight fraction for reproducibility. Figure 3 summarizes the mechanical performance of neat PU and composites comprising 2 wt.% of TiB₂-based fillers. We selected this specific value as the composites prepared at this weight fraction demonstrated an optimal mechanical performance, as explained later. While all TiB₂-based composites exhibit higher stress values compared with neat PU for a given value of strain, the composites fail at a lower strain compared with neat PU (Figure 3a).

To obtain more insights from these stress-strain curves, we inferred the values of Young's modulus (Y), ultimate tensile strength (UTS), strain at break (ϵ_B), and toughness (T) for neat PU and each composite (refer to Table S1, ESI). All TiB₂ based composites exhibit a higher value of Young's modulus compared with neat PU (Figure 3b). While the addition of b-TiB₂ increases the Young's modulus by ~12% (23.39 MPa), the addition of p-NS and f-NS increases the Young's modulus by ~17% (24.43 MPa) and ~43% (29.81 MPa), respectively. Coleman and several other researchers have reported that a high value of Young's modulus in such 2D material- based composites is attributed to the large lateral dimensions of the fillers. ^{52,53} They explained that the failure mechanism of the composite depends on the functional form of the fillers. When external stress is applied to a nanosheet-containing composite, some of the applied stress is transferred to the nanosheets. The intensity of stress transfer depends on interfacial stress transfer and the aspect ratio of the nanosheets. Among all the TiB₂ fillers, f-NS exhibit the largest lateral sizes (as shown earlier in Figures 2c and f), which accounts for the highest value of Young's modulus values for the f-NS-based composites.



Open Access Article. Published on 21 May 2025. Downloaded on 6/5/2025 2:17:29 PM.

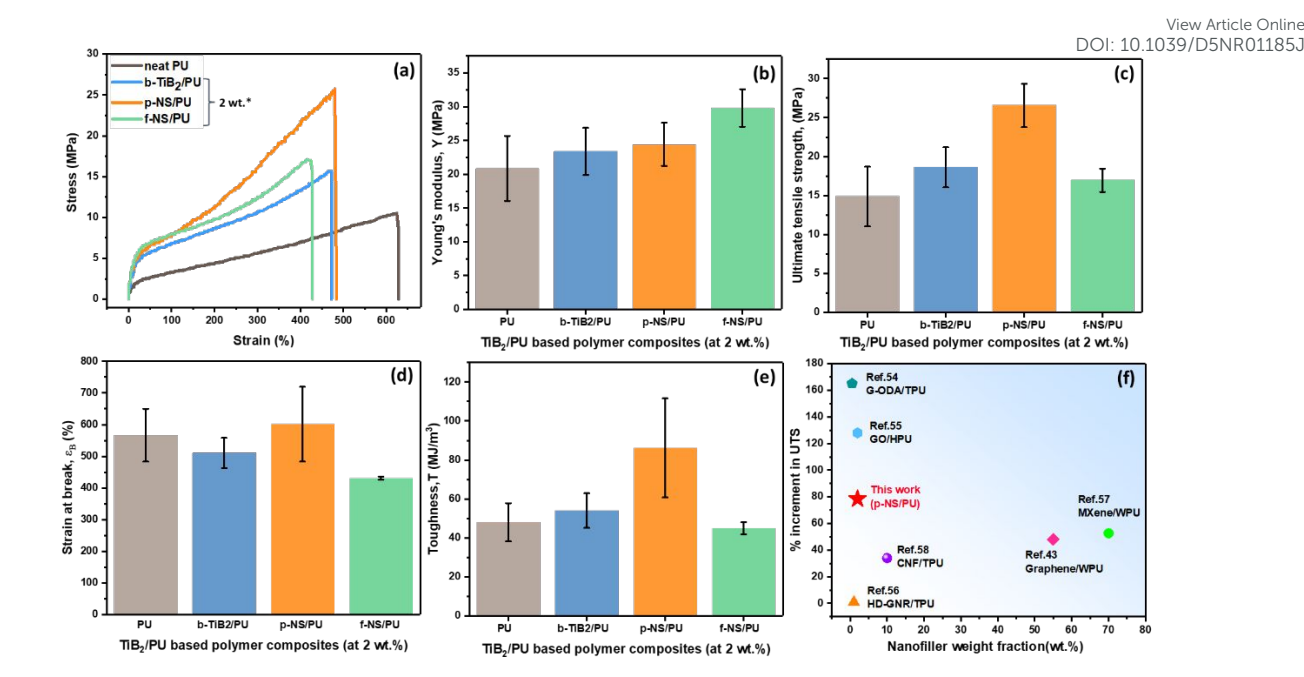


Figure 3. Mechanical properties of neat PU and TiB₂/PU composite films. (a) Stress-strain curve, (b) Young's modulus (Y), (c) Ultimate tensile strength (UTS), (d) Strain at break (ε_B), (e) Toughness (T) (area under stress vs strain curve) as a function of different type of TiB₂ fillers at 2 wt.%), (f) Comparison of the % increment in UTS value after adding different types of fillers in PU matrix, in the literature and the present work.^{43,54–58}

All TiB₂ based composites are also found to exhibit higher values of UTS compared with neat PU (Figure 3c). Among all the samples, the p-NS/PU composite exhibits the highest enhancement in UTS value (24.43 MPa, ~80% increment compared with neat PU). The b-TiB₂ composites also show significant enhancements (~25%), albeit lower than the p-NS-based composites. This result indicates that the 3D structure of b-TiB₂ likely limits its ability to transfer stress as effectively as p-NS, the quasi-2D counterpart of b-TiB₂. This highlights the importance of nano scaling in the context of using TiB₂-based fillers for improving mechanical properties. The f-NS/PU composite exhibits the least improvement in UTS value among all the composites (~14% compared with neat PU). Figure 3d exhibits the strain at break value (ϵ_B) for neat PU and TiB₂/PU composites. These values suggest that the p-NS/PU composite retained the native elastomeric nature of PU to a large extent. However, we observed the lowest ϵ_B value for f-NS/PU, which indicates that f-NS adversely affects the inherent elastomeric nature of PU and makes it brittle (the probable reason for this brittleness is explained later). Toughness values also support the observation drawn from the other mechanical properties

Open Access Article. Published on 21 May 2025. Downloaded on 6/5/2025 2:17:29 PM.

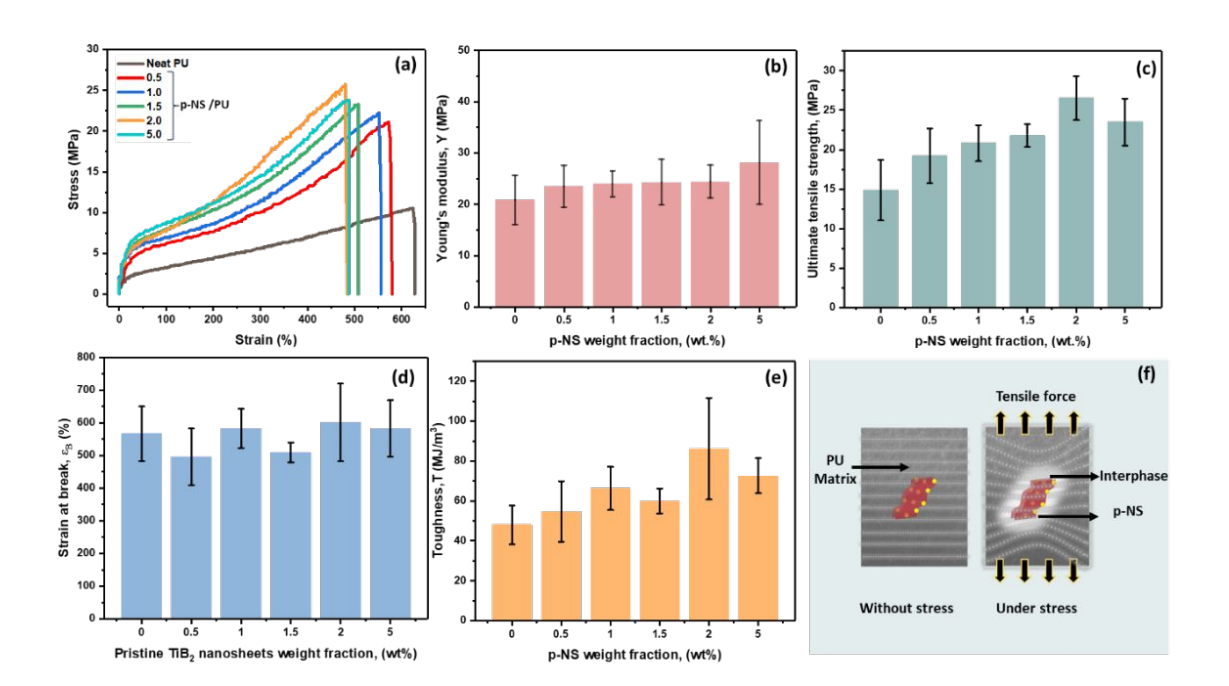
(Figure 3e). Among all other composites, p-NS/PU composite exhibits a maximum toughth sticle Online value of 86.14 MJ/m³, demonstrating an ~80% enhancement compared with neat PU.

We note that while the f-NS-based composites exhibit higher Young's modulus than other composites, they exhibit the least improvement in other specific mechanical properties. This can be ascribed to the presence of functional groups and large lateral dimensions explained as follows. Firstly, the native lattice of TiB₂ is heavily distorted in f-NS due to chemical synthesis, because of which the true potential of boron honeycombs, which endows the exceptional mechanical properties of TiB₂, remains untapped. Secondly, the hydrophilic functional groups on f-NS adversely affect the interaction with the neighbouring hydrophobic polymer. A similar phenomenon has been reported by Andronic and co-workers, where they noted that hydrophilic TiO₂ fillers get agglomerated in a hydrophobic polymer matrix, which weakens the polymer-filler interphase.⁵⁹ Lastly, we observed that when f-NS composites were stretched to their maximum limit, the composites started exhibiting microscopic voids (Figure S8, ESI). Such voids are not visible in b-TiB₂ and p-NS-based composites. These aspects possibly explain why f-NS-based composites exhibited a higher Young's modulus value while not having higher values of UTS, strain at break (ε_B), and toughness values, as these properties primarily represent the behaviour of composite under loading until fracture.

The p-NS composite, on the other hand, was found to have a balanced strength and ductility, resulting in an optimal increment in all specific mechanical properties. Figure 3f summarizes some pertinent values of increment in UTS values from existing literature plotted against the amount of nanofiller required for achieving the respective increments. The p-NS/PU nanocomposite investigated in this work is positioned in the middle-left region of the plot. As we can see, the TiB₂-based fillers outperform other inorganic fillers, such as MXenes, in enhancing mechanical properties. However, graphene with varying functionalization exhibits superior mechanical performance compared with TiB₂-based fillers. For the data set indicated in Figure 3f, we have exclusively considered composites fabricated via the solvent casting method. For a more comprehensive comparison, we have included Table S2 in the ESI that lists the results obtained from mechanical testing of composites fabricated using alternative approaches.

As p-NS-based composites stood out among all the TiB₂-based composites, we tested the dependence of mechanical properties of this composite on the p-NS weight fraction. Six

filler fractions were chosen, namely, 0, 0.5, 1, 1.5, 2, and 5 wt.%. Figure 4a depicts the telegraphic response of neat PU and p-NS/PU composites as a function of the filler fraction.



This article is licensed under a Creative Commons Attribution 3.0 Unported Licence

Open Access Article. Published on 21 May 2025. Downloaded on 6/5/2025 2:17:29 PM.

Figure 4. Mechanical properties of neat PU and p-NS/PU composite. (a) Stress-strain curve, (b) Young's modulus (Y), (c) Ultimate tensile strength (UTS), (d) Strain at break (ε_B), (e) Toughness(T) (area under stress vs strain curve), as a function of p-NS weight fraction, (f) Depiction of stress transfer at nanosheet-polymer interphase, by showcasing the changes in the deformation patterns under stress.

To obtain deeper insights from the stress-strain curves, we inferred specific mechanical properties of the composites at various weight fractions. Figure 4b depicts the Young's modulus values as a function of p-NS wt.%. The modulus for neat PU is 20.85 MPa. It is found to increase monotonically with an increase in the filler fraction. The modulus for the 5 wt.% p-NS composite is found to be 28.12 MPa, that is ~35% higher than the neat PU case. These increments indicate that p-NS can significantly enhance the stiffness of PU.

Figure 4c depicts the UTS values as a function of p-NS wt.%. The UTS of neat PU is found to be 14.8 MPa. It increases to 19.20 MPa upon adding a mere 0.5 wt.% of p-NS (~20% enhancement) and to 26.55 MPa upon adding 2 wt.% of p-NS (~80% enhancement). However, beyond 2 wt.%, the UTS exhibits a decremental trend, possibly due to the aggregation of nanosheets within the PU matrix. Such an effect of agglomeration has also been shown previously by Coleman and coworkers.⁴³

Open Access Article. Published on 21 May 2025. Downloaded on 6/5/2025 2:17:29 PM.

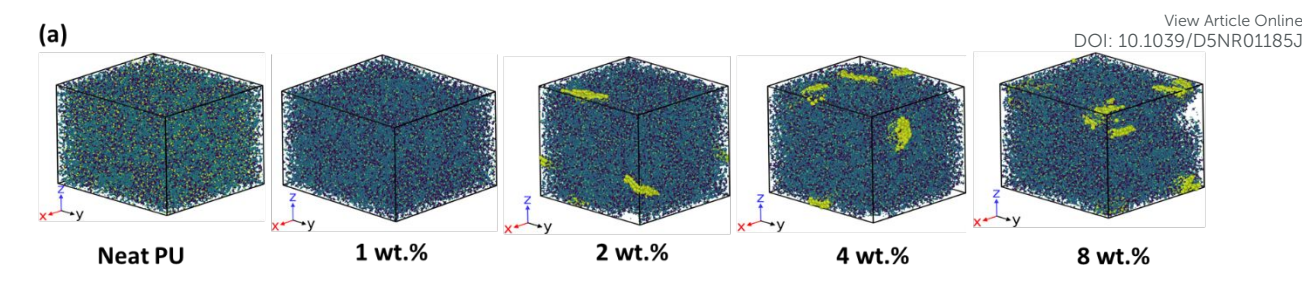
Figures 4d and e depict the strain at break (ϵ_B) and toughness, respectively. While the strain at break values do not exhibit a particular trend with increasing weight fraction of p-NS, these indicate that the composite comprising 2 wt.% of p-NS exhibits optimal mechanical performance, and we can develop a stiff, strong, yet tough composite. This is the reason we selected the value of 2 wt.% to compare the effect of different TiB₂-based fillers (Figure 3). The additional datasets we obtained at other filler fractions (0, 0.5, 1, 1.5) for b-TiB₂ and f-NS fillers are shown in Table S1, ESI.

It is curious to understand how the presence of nanosheets of TiB₂ fillers renders superior mechanical properties to the PU matrix. It is known that the interphase (which is formed when fillers are added to a polymer matrix) and the inherent nature of fillers play an important role in the mechanical performance of composites.¹⁶ We envisage a similar mechanism at play for the composites we prepared using TiB₂ fillers (Figure 4f). To gain a better understanding of this phenomenon, we carried out computational studies as well as detailed physicochemical characterization. We first explain the insights obtained from simulations, and follow it up with the inferences from physicochemical studies.

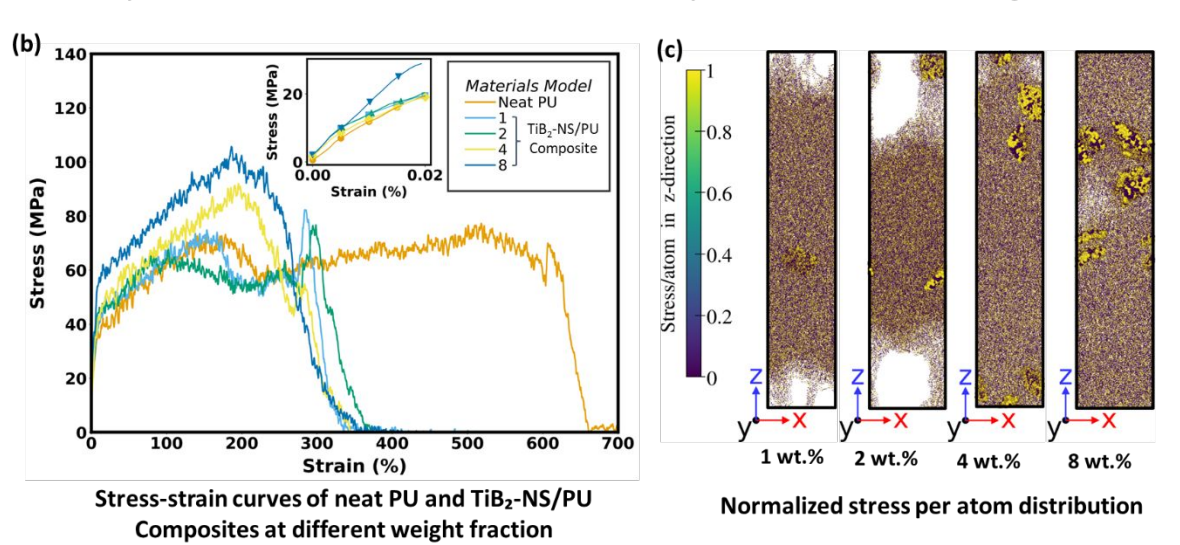
Insights from molecular dynamics (MD) simulations: There are only a few computational studies available in the literature to model the structure and deformation behaviour of PUs. Rutledge and coworkers ^{60,61} utilized the Interphase Monte Carlo (IMC) method to model thermoplastic polyurethane (TPU) chains in their semicrystalline form and provided a foundation for correlating structural changes with macroscopic mechanical properties. ^{60,61}These studies revealed the mechanism behind the deformation behaviour of PU and highlighted the complex response of PU under loading conditions owing to the interplay of hard and soft segments. Notably, the enhancement of mechanical properties and interfacial deformation mechanisms for PU-based composites are poorly understood.

We developed bulk models for neat PU and four composites comprising different filler fractions of TiB₂ nanosheets (1, 2, 4, and 8 wt.% of TiB₂ nanosheets) and subjected them to tensile deformation. While modelling, we modelled PU chains as amorphous because experimentally, we found that the degree of crystallinity of PU and composite is very low, as explained later using DSC data.

Figure 5a shows the equilibrated structures of PU and the composite models. The equilibrium densities of composites showed a monotonic increase with the filler fraction. For example, the density increased from 0.91 g/cm³ for neat PU to 1.08 g/cm³ for the 8% TiB₂ NS/PU composite (see Figure S9 and Table S3 for details in ESI).



Equilibrated structures of neat PU and TiB2-NS/PU composite models at different weight fraction



Open Access Article. Published on 21 May 2025. Downloaded on 6/5/2025 2:17:29 PM.

Figure 5. MD simulations of neat PU and Composites of different weight fractions. (a) Equilibrated structures of PU and composites models (1, 2, 4 and 8 wt.% TiB_2 -NS), (b) stress-strain curves of neat PU and composites as a function of TiB_2 -NS weight fraction, (c) Stress per atom distribution in TiB_2 -NS/PU composites along z-direction at a strain of 3.

Figure 5b shows the stress-strain curves obtained during tensile deformation simulations with a strain rate of 10⁹ s⁻¹. For neat PU, we observed significant plastic deformation, sustaining elongation up to a strain of 7. This extensive plastic deformation can be attributed to two primary mechanisms – first, the unfolding of polymer chains and, second, their alignment and stretching along the tensile direction. We observe that the obtained value of Young's modulus of neat PU (613.6 MPa) is lower than the values reported by Zhu et al.,⁶¹ for semicrystalline PU and by Talapatra et al.⁶² who reported a modulus of 0.98 GPa for neat amorphous PU. We also note that the modulus calculated from our MD simulations is an order of magnitude higher than our experimental values owing to several well-known reasons, such as the choice of the interatomic potentials, the representative model structures themselves (smaller chain lengths and different chain chemistries) and much higher strain rates compared to experiments (due to the limitations in terms of timescales that can be simulated using MD).⁶³ Notwithstanding these limitations, MD

Open Access Article. Published on 21 May 2025. Downloaded on 6/5/2025 2:17:29 PM.

This article is licensed under a Creative Commons Attribution 3.0 Unported Licence.

offers a powerful means to understand the reinforcement mechanisms. The Young's modulity of the Continuous and the reinforcement mechanisms. composites calculated from MD simulations showed a consistent increase with higher TiB₂-NS weight fractions, indicating improved stiffness in the composites (refer to inset 5b). This trend is consistent with our experimental findings. With higher TiB₂-NS weight fractions, the PU polymers adhering to the surface of TiB₂ nanosheets undergo unfolding and stretching, leading to void formation near the nanosheets. This behaviour is attributed to the weak Lennard-Jones (LJ) potential at the polymer-TiB₂ interface. Despite the distortion of TiB₂ nanosheets during deformation, they contribute significantly to the reinforcement of the composite, as highlighted in Figure 5b. Furthermore, as the TiB₂ content increases, the strain at which failure occurs decreases, indicating reduced ductility. However, this is accompanied by a notable increase in Young's modulus and yield strength, emphasizing the trade-off between stiffness and elongation at break in these composites, in accordance with our experimental observations. The mechanical properties for all the structures modeled are summarized in Table S3. These simulated results are also in accordance with our experimental results. It is to be noted that there are quantitative differences with respect to our experimental measurements due to the aforementioned factors in the simulations; however, the trends for the mechanical behavior agree quite well with experiments.

In Figure 5c, we show how the stress per atom is distributed for the various structures at a strain of 3. The colour bar represents the magnitude of stress per atom on a scale of 0 to 1. This shows that TiB₂ nanosheets actively take part in stress distribution, an essential requirement for enhancement of mechanical properties. For more insights, we captured the snapshots of the deformation at a strain of 3 for neat PU, 4 wt.%, and 8 wt.% TiB₂-NS/PU composite (Figure S10, SI). These snapshots provide visual evidence of the changes induced by TiB₂ nanosheets in the PU matrix. We observed that the neat PU depicts a highly anisotropic deformation behaviour (see Figure S10, SI). At the strain of 3, the cavitation occurs only in one direction (along *y*-axis), while elongation continues along the *x*- and *z*-directions. This indicates that the orientation of the hard and soft segments has a strong role in load-bearing during extension. However, this effect is expected to be much lesser in our experimental samples. For TiB₂-NS/PU composites, the anisotropy decreased significantly with increasing TiB₂-NS weight fractions due to the presence of the fillers and the ensuing interfacial interactions with PU. We also note that varying the aspect ratio of the TiB₂-NS offers further scope for optimization of the mechanical properties.

Physicochemical characterization: To gather deeper insights into the interphase formed between the fillers and the polymer matrix and to quantify the nature of polymer/filler

Open Access Article. Published on 21 May 2025. Downloaded on 6/5/2025 2:17:29 PM.

This article is licensed under a Creative Commons Attribution 3.0 Unported Licence

interactions, we recorded the FTIR spectra of neat PU and composites (Figure 6a). The PTIR Spectra of neat PU exhibit five primary bands – 3330 cm⁻¹ (hydrogen-bonded N-H stretching vibration), 2959 cm⁻¹ (asymmetric CH₂ stretching), 1729 cm⁻¹ (stretching vibration of free carbonyl group), 1699 cm⁻¹ (stretching vibration of H-bonded carbonyl group), and 1526 cm⁻¹ (C-N stretching). Compared with neat PU, we observed a gradual decrease in the intensity of the bands for b-TiB₂/PU and p-NS/PU composites (refer to Table S4, ESI). This decremental trend of the b-TiB₂/PU and p-NS/PU composites indicates that these fillers chemically interact with the PU matrix. F4.64 However, for f-NS/PU composites, we observed no significant change in the intensity compared with neat PU, which suggests that f-NS do not interact well with the PU matrix. This also explains the decrease in the mechanical performance of f-NS-based composite compared with other TiB₂ composites. However, one recent report exhibits that these f-NS nanosheets interacted well with bio polymer⁶⁵, but the studied polymer was hydrophilic in nature. This underscores the importance of considering the wetting characteristics of both fillers and the polymer during composite preparation.

To quantify this degree of interaction, we chose the carbonyl stretching region (1672-1761 cm⁻¹). This region indicates the formation of hydrogen bonds between hard segments. We calculated the hydrogen bonding index (HBI) and degree of phase separation (DPS). To calculate HBI values, we measured the intensity ratio of the H-bonded carbonyl band to the free carbonyl band. The method to calculate HBI and DPS is shown in ESI under Section S12.

The HBI values, as shown in Table 1, were obtained using the carbonyl region as shown in Figure S11 in the ESI. We note that for b-TiB₂ and p-NS filler-based composites, the HBI value was slightly reduced. This suggests that such fillers might be non-covalently attached to the PU matrix and hence restrict the motion of the hard segment.⁶⁶ The composites also exhibit slightly lower DPS values compared with neat PU, which indicates that these fillers hinder the phase separation of hard and soft segments. Additionally, we did not observe any new band for composites, which signifies the well-distributed fillers in the polymer matrix.

Table 1: Calculation of hydrogen bonding index (HBI) and degree of phase separation (DPS)

Samples	I ₁₆₉₉	I ₁₇₃₀	НВІ	A ₁₆₉₉	A ₁₇₃₀	DPS
Neat PU	36.61	43.71	83.76	13.51	18.41	0.73
b-TiB ₂ /PU	26.28	33.58	78.26	11.37	17.9	0.64

p-NS/PU	20.25	27.77	72.92	11.53	17.11	View Art DOI: 101939/D5N	cle Online IR01185J
f-NS/PU	34.72	41.22	84.23	13.28	18.87	0.70	

To obtain some physical insights, we studied the cross-sectional FE-SEM images of the fractured surface of neat PU and TiB₂/PU composites (Figures S12 and S13). The FE-SEM image of neat PU film depicts the smooth surface without any fractures (Figure S12a). In contrast, the FE-SEM images of composites exhibit rough surfaces. Particularly, the fractured surface of b-TiB₂/PU and p-NS/PU composites depicts a small number of fillers on the surface (as shown in Figures S12b, c), which indicates a strong interaction of these fillers with the polymer. However, we observed several nanosheets protruding outwards in the case of f-NS/PU composite, which indicates a weaker interaction of f-NS with PU (Figure S12d). Tensile testing and FTIR results also corroborate these inferences.

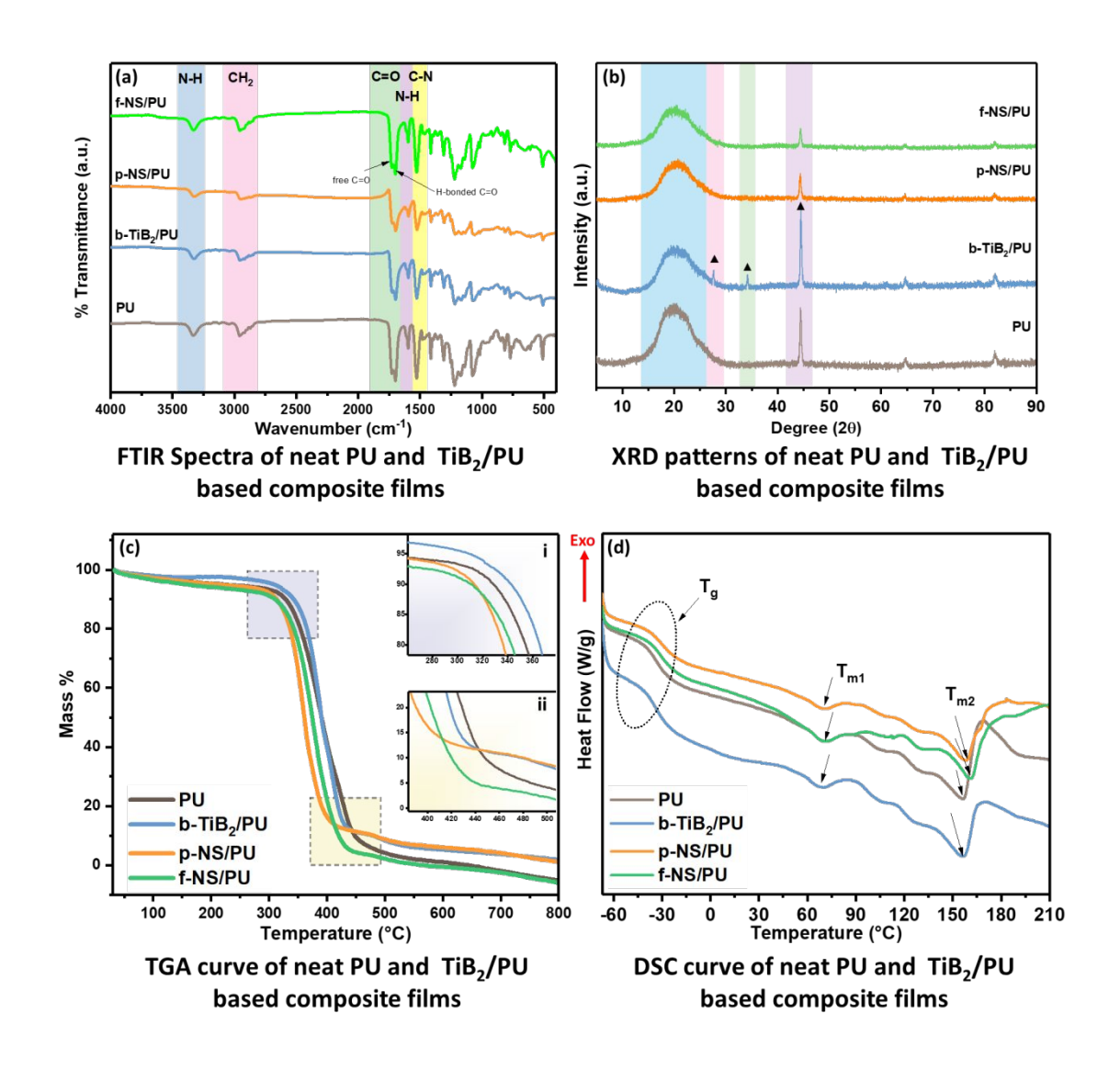


Figure 6. Chemical and thermal characterization of neat PU and its composites at 2 12 185 [Definion of TiB₂ based fillers. (a) FTIR spectra depict a reduction in intensity for b-TiB₂ and p-NS-based composites compared with neat PU, reflecting an interaction between these fillers and PU, which is not evident in an f-NS-based composite. (b) XRD patterns exhibit no significant change in the crystal structure of native PU; (c) TGA and (d) DSC curves also demonstrate the changes in the thermal characteristics for composites compared with neat PU, representing an interaction between TiB₂-based fillers and PU.

We also investigated the changes in crystal structures in the PU matrix after incorporating TiB₂-based fillers. Figure 6b shows the XRD patterns of neat PU and its composites. The PU exhibits primarily two peaks at 19.98° and 44.38°. The first peak represents the short-range ordered structure of hard and soft segments, ^{67,68}, and the second peak represents the oriented hard domains. TiB₂/PU composites exhibit a reduction in the first peak with respect to neat PU. This is due to the interaction between the polymer and filler, which disrupts the typical molecular arrangement of PU. Moreover, specifically, in the b-TiB₂/PU composite, two new peaks emerge at 27.67° and 33.97°, which indicates the presence of (001) and (100) plane of b-TiB₂ (shown by a triangle in Figure 6b). The possible reason behind the emergence of those peaks in b-TiB₂/PU composites is the highly crystalline structure of b-TiB₂, as shown in the XRD pattern (Figure 2h). Moreover, there is an increment in the intensity of the 44.38° peak due to an overlapping of the (101) peak of b-TiB₂. We did not observe any new peak in the case of p-NS and f-NS-based composites because of their weak crystallinity compared with b-TiB₂ (as shown in XRD patterns, Figure 2h).

To obtain insights on the strength of the bonds between fillers and matrix, we performed TGA-DSC analysis on neat PU and TiB₂/PU composite. Figure 6c shows the TGA curve of neat PU and the composite films at 2 wt.% loading. As shown, neat PU and its composites exhibit a two-stage decomposition behaviour. The first stage ranges from 283°C to 440°C, which occurs due to urethane bond decomposition. The second stage is between 450 °C to 653 °C, which occurs due to decomposition of the polyol segment and thermo-oxidative degradation of the polyurethane backbone. We measured the temperature at 10% and 90% wt. loss of the initial sample, representative of the changes in both decomposition stages, as shown in Table S5, ESI. For b-TiB₂/PU composites, we observed a significant temperature shift compared with neat PU. For instance, the temperature for 10 wt.% loss (T_{10%}) is shifted from 328 °C to 342 °C, and the temperature for 90 wt.% loss (T_{90%}) is shifted from 448 °C to 482

Open Access Article. Published on 21 May 2025. Downloaded on 6/5/2025 2:17:29 PM.

°C. This temperature shift indicates that b-TiB₂ particles likely delay the decomposition of Particle Online bonds. For p-NS/PU composites, we observed no shift for 10 wt.% loss (T_{10%}), and a significant shift in the T_{90%} (shifted from 448 °C to 482 °C). This temperature shift is similar to b-TiB₂-based composites and ascribes to the fact that the b-TiB₂ and p-NS fillers restrict the motion of the polymer. Thakur et al. found that the restrictive motion of polymer chains can be attributed to robust physicochemical interactions between filler and polymer. In contrast, f-NS/PU composites exhibit a negative shift in temperature compared with neat PU for both wt.% losses. This observation confirms the lack of interaction between f-NS and neat PU, which is consistent with the FTIR and tensile testing results. The increase in the residual amount at 600 °C also indicates that the addition of b-TiB₂ and p-NS improves not only the mechanical properties but also the thermal properties.

Further, we employed DSC to gather insights about the changes in the melting and crystallization behaviour because this is also influenced by the interaction of these TiB2-based fillers with PU. In Figure 6d, we have shown the DSC thermograms of neat PU and TiB₂/PU composites. We determined the glass transition temperature (T_{σ}) and melting temperature (T_{m}) of neat PU and its composites from DSC thermograms, as shown in Table S6 in ESI. It is visible that the T_g value of p-NS and f-NS-based composites increased in comparison to neat PU. However, for b-TiB₂-based composites, T_g remains the same, likely due to the agglomeration of b-TiB₂ fillers at T_g, facilitating an easier movement of polymer chains. Unlike b-TiB₂, the decrement in the Tg value of p-NS and f-NS-based composites suggests reduced molecular motion of PU chains due to these fillers. Moreover, we observed two melting endotherms –T_{m1} and T_{m2} in neat PU and composites. We observed no significant change in the T_{m1} value, as shown in Table S6, ESI. However, we observed a significant incremental change in T_{m2} value after adding TiB2-based fillers. The changes in Tm values also signify the interfacial interaction between fillers and PU, which is attributed to the reduced molecular motion of PU chains. Additionally, we calculated the % crystallinity (χ_c) and found that neat PU and composites remain mostly amorphous (Table S6). In simulation, we built our PU model as amorphous using this information.

The work reported here presents a systematic investigation of the candidacy of TiB₂-based fillers in reinforcing the mechanical properties of a polymer. This study highlights that reinforcing the mechanical properties of the polymer depends on the filler geometry, filler-matrix interphase, and Young's modulus of fillers itself explained as follows.⁶⁹

Filler geometry and filler-matrix interaction. We found that p-NS-based composites demonstrated better mechanical performance than b-TiB₂-based composites, which is attributed to the 2D geometry of the p-NS, facilitating a more effective stress transfer than three-dimensional b-TiB₂. However, f-NS, despite having the 2D geometry, exhibits only nominal enhancement in mechanical performance of PU. This is attributed to their incompatibility with base polymer and distorted crystal lattice, which affects the strength of the interphase. As we know, if the filler-polymer interphase is not strong enough to withstand applied stress, it results in poor stress transfer.

Young's modulus of fillers. The improvement in the mechanical properties of composites also depends upon the intrinsic mechanical properties of fillers, which are primarily measured by Young's modulus. If the modulus of fillers is high compared with polymer, shear stress would be induced at the filler/PU interphase. Consequently, the filler would bear most of the applied stress, resulting in better mechanical properties. We observed an improvement in the mechanical properties of the b-TiB₂/PU composite despite it having a three-dimensional geometry (although it was lower than the p-NS/PU composite). The improved mechanical properties of b-TiB₂ is also because of the high Young's modulus, ~565 GPa.³⁴ Such a high value of Young's modulus is attributed to the unique graphenic arrangement of boron atoms in between the titanium metal, as shown in Figure S14, ESI.⁷⁰ However, Young's modulus of nanosheets synthesized from b-TiB₂ has not been reported so far. Still, we can assume that if their intrinsic graphenic arrangement remained intact during nano scaling, the modulus would increase significantly, similar to graphene.⁷¹ This assumption aligns with the observed enhancement in the mechanical properties of p-NS/PU composites – as p-NS is the 2D counterpart of b-TiB₂, in which the native lattice of TiB₂ is retained to a large extent. However, during the synthesis of f-NS, the chemical synthesis route distorts the native lattice of TiB₂, which probably caused a decrease in Young's modulus of these nanosheets. This is also one of the reasons behind the decrease in the overall mechanical response of f-NS/PU composites.

Conclusions:

To sum up, we demonstrate that quasi-2D nanostructures from TiB_2 can lead to a significant enhancement in the mechanical properties of polyurethane, even at low-weight fractions. We show that an enhancement of up to ~80% in the UTS and toughness can be obtained by adding pristine nanosheets of TiB_2 to PU. A vis-à-vis comparison of composites prepared using functionalized nanosheets of TiB_2 indicates that this enhancement is closely linked to the nature of interphase formed between the PU matrix and TiB_2 nanofillers. We acknowledge that certain

trade-offs are associated with the addition of TiB₂-based fillers. While all TiB₂-based fillers are found to improve the tensile strength of PU, the b-TiB₂ and f-NS fillers are associated with a more pronounced reduction in flexibility compared with the p-NS filler. Additionally, while b-TiB₂ and p-NS improved thermal stability, the inclusion of f-NS adversely affects the thermal stability, highlighting the critical role of the native metal boride lattice in determining composite performance. We also obtained computational insights to understand how nanoscaled TiB₂ fillers render superior mechanical properties to the PU matrix. Simulations reveal that TiB₂ nanosheets not only actively contribute to load distribution but also promote isotropic mechanical behaviour. This study highlights the potential of TiB₂-based nanofillers in reinforcing polymer matrices. We also showcase how hydrogen bonding varies with the inclusion of different variants of TiB₂-based fillers within PU matrix. It would be promising to explore temperature-dependent changes in hydrogen bonding in these composite films. The multi-functional nature of TiB₂-based nanosheets makes such composites useful for diverse applications such as flexible electronics, energy storage systems, and medical devices.

Methods:

This article is licensed under a Creative Commons Attribution 3.0 Unported Licence

Open Access Article. Published on 21 May 2025. Downloaded on 6/5/2025 2:17:29 PM.

Synthesis of TiB2-derived pristine nanosheets

TiB₂-derived pristine nanosheets (p-NS) were synthesized as reported in our recent work³⁰ using high-energy ball milling (Dual Mixer/Mill 8000D from SPEX SamplePrep). In a single batch, ~1.3 g of TiB₂ powder (Sigma-Aldrich, 99.5% pure, particle size <10 μm) was added to the zirconia vial (ZrO₂) along with ZrO₂ balls in order to maintain a 20:1 ball-to-powder ratio (BPR). After adding balls and TiB₂ powder, the vial was sealed with an O-ring to prevent loss of material during the milling process. After that, the vial was loaded into the mill. One more empty vial was loaded in the opposite slot of the ball mill to maintain equal weight at both ends. The run was performed for 6h to achieve complete exfoliation. After completion of the run, milled powder comprising of nanosheets was scrapped from the vial and stored in a desiccator.

Synthesis of functionalized TiB₂ Nanosheets

TiB₂-derived functionalized nanosheets (f-NS) were synthesized using the dissolution and recrystallization approach as reported previously by our group.³² Briefly, 300 mg of TiB₂ powder (Sigma Aldrich, 99.5% pure, size $<10 \mu m$) was added to 90 mL of deionized water and stirred at 250 rpm for 10 minutes to form a black suspension. Then, in this black suspension, 10 mL of hydrogen peroxide (H₂O₂) (Merck, 30%) was added dropwise. After continuous

stirring for 1h, the suspension gradually turned yellow in color. The suspension was yellow undisturbed for 24 h, after which the yellow top phase was collected and centrifuged at 8000 rpm for 30 minutes at 20°C. After centrifugation, the supernatant was collected and frozen at -4°C for 24 h. This frozen sample was subsequently lyophilized (Martin Christ Alpha-2D Plus) for 72 hours, which resulted in a pale-yellow fluffy powder comprising functionalized nanosheets.

Preparation of polymer composites using TiB2-based fillers

Polyurethane (PU) composites with different wt.% of TiB₂-based fillers were prepared using the solution casting method. In the first step, PU beads (Estane® 5707 TPU, refer section 17, ESI for more details) were dissolved in dimethyl formamide (DMF) (Emplura, 99% pure) by stirring them at 150 rpm for 3 h at 80 °C to obtain a 75 mg/ml polymer stock solution. In the second step, TiB₂-based fillers (at different wt.% – 0.5%, 1%, 1.5%, 2%, and 5%) were dispersed in an appropriate amount of PU stock solution and DMF solvent. The amount of each component was adjusted such that the final dispersions have the same weight and same volume (600 mg and 30 mL, as explained in Table S7 in ESI). These dispersions were obtained by stirring at 250 rpm for 5 min, followed by bath sonication of 1 min. In the third step, this dispersion was poured into glass petri dishes, placed in a vacuum oven, and dried at 60°C for 96 h to evaporate the solvent. In the final step, the dried composites were allowed to cool at room temperature, following which films were carefully peeled off using tweezers, shown in figure 1(a-f). We used three types of TiB₂ fillers for the preparation of TiB₂/PU composite. By following the same procedure, we prepared triplicates of each sample for further analysis.

Tensile testing of composite films

After peeling off the films, the samples were cut into rectangular specimens measuring 2.5 cm x 6 cm. These rectangular test specimens were clamped in a Universal Testing Machine (UTM) (NTF computerized tensile strength tester) for tensile testing. After clamping, a specimen was stretched at a constant crosshead speed of 100 mm/min. The stress and strain values were calculated using the following expressions.

$$Stress = \frac{Load}{Cross-sectional\ area}.$$
 (1)

$$Strain = \frac{Displaced\ length}{Original\ length}$$
 (2)

Young's modulus was calculated by selecting the linear region of the stress-strain plot. Selected data points from the linear region were replotted and fitted using a linear fit function

Open Access Article. Published on 21 May 2025. Downloaded on 6/5/2025 2:17:29 PM.

in Origin software. The slope of the linear fit corresponds to Young's modulus. For each $\frac{\text{Very Article Online}}{\text{DSNR01185J}}$ of sample, at least three samples were tested to ensure the accuracy of measured properties. We expressed all the mechanical properties as mean \pm standard deviation.

Field Emission Scanning Electron Microscopy (FE-SEM)

Field Emission Scanning Electron Microscopy (FE-SEM) images of fillers and composite films before and after fracture were captured using JEOL JSM 7600F instrument. The instrument was operated at 3 kV with a working distance of 8 mm. For imaging, the powder sample was dusted on carbon tape, while composite films were directly used after being cut into 0.5 cm × 0.5 dimensions. After mounting on SEM stubs, the samples were coated with platinum for about 80 s.

Transmission Electron Microscopy (TEM)

Transmission Electron Microscopy (TEM) images of nanofillers and composite films were obtained using a Thermo Scientific Themis 300 instrument operated at 300 kV. For imaging TiB₂ fillers, samples were prepared as follows—1 mg/mL suspension of powder form of nanosheets in DI water was prepared using bath sonication for 10 min (Bandelin Sonorex Digitec, 140 W, 35 kHz). This suspension was further diluted 100X, and from that, 15 μL of this diluted suspension was drop cast onto lacey carbon Cu grids (Ted Pella, 300 mesh). For imaging nanocomposite, ultra-thin sections (less than 100 nm) of the composite film embedded in the epoxy, were prepared using an ultramicrotome (Leica, Ultracut EM FC6). These ultra-thin sections were transferred onto the lacey carbon Cu grids (Ted Pella, 300 mesh). The obtained images were further processed using GATAN software.

Atomic Force Microscopy (AFM)

Atomic force microscopy (AFM) images of nanofillers were obtained using Bruker NanoWizard Sense AFM instrument operated in tapping mode using a Sb-doped silica cantilever (spring constant = 3 N/m, resonating frequency = 75 kHz). Briefly, 1 mg/mL suspension of powder form of nanosheets in DI water was prepared using bath sonication for 10 min (Bandelin Sonorex Digitec, 140 W, 35 kHz). This suspension was diluted 200X, and 10 μL of that diluted suspension was drop-cast on a freshly cleaved mica substrate followed by drying in desiccator for 24 h. The obtained images were processed using JPK NanoWizard Sense+ software.

Fourier-Transform Infrared Spectroscopy (FTIR)

Fourier transform infrared Spectroscopy (FTIR) of TiB₂-based fillers and composite films we filler online collected using a Spectrum Two, PerkinElmer instrument. The scanning was performed in the range of 400 to 4000 cm⁻¹.

X-ray Diffraction (XRD)

X-ray diffraction (XRD) analysis of TiB₂-based fillers was performed using D8 DISCOVER (Bruker) instrument, whereas a Multipurpose X-ray diffractometer (SmartLab, Rigaku Corp., Japan) was used to measure composite films using Cu K α -radiation (λ = 1.54 Å). For the analysis, the scan range was set from 5° to 90° (in 2 θ). After collecting the data, we analyzed the data using an ICDD data file-TiB₂:00-351-0741.

X-Ray Photoelectron Spectroscopy (XPS)

X-ray photoelectron spectroscopy (XPS) data of composite film were recorded using the Thermofisher Scientific Nexsa base model using monochromatic Al K α as a source with 1486.6 eV energy. Recorded data was baseline corrected and deconvoluted using origin software.

Thermal behaviour Analysis

Thermogravimetric analysis (TGA) of composite films was performed using a Perkin Elmer TGA system, and differential scanning calorimetry (DSC) analysis of composite films was measured using the TA-instrument DSC 5000 system. For TGA, the temperature was varied from 30 °C to 800 °C with a nitrogen (N_2) flow rate of 10 mL/min. The initial weight of the sample for TGA was ~2 mg. For DSC, the temperature was varied from -70 °C to 150 °C with N_2 flow rate of 10 mL/min. The initial weight of the sample for DSC was ~10 mg.

Dynamic Mechanical Analysis (DMA)

Dynamic Mechanical Analysis (DMA) of composite film was performed using TA-instrument DMA 850. The temperature was varied from -70 °C to 150 °C with a heating rate of 5°C/min at a constant vibrational frequency of 1 Hz. The sample dimensions for the analysis were 3.5 cm×0.6 cm.

Model Construction and Simulation.

For our Molecular Dynamics simulations of the composite, the initial simulation setup comprising multiple PU chains was modeled using the MedeA simulation package.⁷² Energy

Open Access Article. Published on 21 May 2025. Downloaded on 6/5/2025 2:17:29 PM.

minimization was carried out on a large simulation cell that contained sufficient spaces between the PU chains. All interactions between the chains were described using the recent version of the polymer consistent force field (*pcff+*), which includes detailed parameters for bonded interactions (bond stretching, angle bending and dihedral interactions) and non-bonded interactions (van der Waals and electrostatic forces). The information on the functional form of the *pcff+* force field is mentioned in section S19, ESI. The PU chains modeled in this study consisted of four hard segments (MDI/BDO) at either end, and 24 soft segments (PTMO) in the center, maintaining a hard-to-soft segment ratio of 1:3. To elucidate the atomistic deformation mechanisms and highlight the qualitative variation of the mechanical behavior as observed in our experiments, we consider neat PU and nanosheets of TiB₂ as reinforcement in TiB₂-NS/PU composites with varying weight fractions of the nanosheets. Fully periodic (bulk) models of neat PU and TiB₂-NS/PU composites were developed and subjected to tensile testing using the LAMMPS (Large-scale Atomic/Molecular Massively Parallel Simulator) simulation package.⁷³

All systems consisted of a total of 256 PU chains comprising 127,656 atoms. The amorphous PU matrix was generated by heating the system to 800 K for 300 ps using the Nosé-Hoover thermostat and barostat, well above its glass transition temperature. The system was then cooled to room temperature (300 K) at a rate of 1 K/ps and equilibrated under anisotropic NPT conditions at 300 K and 1 atm for 2 ns to achieve the target density of 0.91 g/cm³. Tensile deformation was carried out on the equilibrated systems at a strain rate of 10° s⁻¹, up to a total strain of 900%. The TiB₂-NS is modeled with an aspect ratio of 1:4, based on an 8×8×2 TiB₂ supercell derived from the unit cell of TiB₂ provided in the Materials Project database. The 1:4 aspect ratio is taken as per the value reported in the literature for TiB₂-based nanosheets) We employed the modified embedded atom method (MEAM) potential to model the pairwise interactions of TiB₂. Toses-interaction parameters between the polymer and TiB₂ were defined using Lennard-Jones (LJ) parameters and the Lorentz-Berthelot mixing rule. The LJ parameters for Ti and B atoms taken for the cross interactions with PU were those from the MEAM potential.

The equilibration protocol for the composites followed a similar protocol as the neat PU (heating to 800 K and subsequently cooled to 300 K to generate an amorphous PU matrix with embedded TiB₂ nanosheets). Following anisotropic equilibration under NPT, tensile testing was conducted at a strain rate of 10⁹ s⁻¹ until failure.

View Article Online

DOI: 10.1039/D5NR01185J

Supporting Information

Information about TiB₂/PU Composite preparation. AFM images of TiB₂-based fillers. Additional characterization of TiB₂/PU composites-FESEM, TEM, DMA, XPS, FTIR, and TGA-DSC. Crystal structure of TiB₂. Mechanical properties of neat PU and TiB₂/PU composite films, Equations used for simulation model construction, Equilibration plots, and Stress-strain curves of simulated models.

Conflict of Interest

The authors declare no conflicts of interest.

Data availability

This article is licensed under a Creative Commons Attribution 3.0 Unported Licence

Open Access Article. Published on 21 May 2025. Downloaded on 6/5/2025 2:17:29 PM.

The data supporting this article have been included as part of the Electronic Supplementary Information (ESI).

Acknowledgment

We sincerely acknowledge the Central Instrumentation Facility (CIF) at IIT Gandhinagar for providing access to various instruments that were essential for our characterization work. We also extend our gratitude to CRF-IIT Delhi for facilitating TEM, DSC, and DMA analyses and to AMRC-IIT Mandi for supporting us with XPS analysis. K.J. acknowledge the funding received from the seed grant IITGN, Core Research Grant (No. CRG/2023/008191) awarded by SERB India, STARS Research Grant (No. MoE-STARS/STARS-2/2023-1024) by Ministry of Education, India, and financial support from the Dr. Dinesh O. Shah Chair Fellowship. We also acknowledge the Department of Scientific and Industrial Research (DSIR) for enabling the use of the Common Research & Technological Development Hub (CRTDH) facility (Grant DSIR/CRTDH/NM/IIT-Gn/2016), and DST-FIST grant [SR/FST/ET-I/2020/554]. R.R. acknowledges the supercomputing facility of IIT Gandhinagar (Param Ananta) and NIT Trichy (Param Porul) for all the simulations and funding support from the Core Research Grant (No. CRG/2023/005333). The authors wish to especially thank Dr. Krishna Kanti Dey for kindly allowing us to use the vacuum oven, Dr. Abhijit Mishra and his student Prathmesh Bhadane for their assistance with the UTM, and Anshul Rasyotra for his valuable insights in designing the experiments. We also want to thank our Chemical Department office staff members – Mr.

Open Access Article. Published on 21 May 2025. Downloaded on 6/5/2025 2:17:29 PM

Suvakanta, Mr. Rajib, Mr. Supresh, and Mr. Rohit – for their prompt assistance in processing included in processing in processin

References

- 1 K. S. Novoselov, A. K. Geim, S. V Morozov, D. Jiang, Y. Zhang, S. V Dubonos, I. V Grigorieva and A. A. Firsov, *Electric Field Effect in Atomically Thin Carbon Films*, Kluwer, 2000, vol. 404.
- 2 A. K. Geim and K. S. Novoselov, *Nat. Mater.* 2007 63, 2007, **6**, 183–191.
- S. Z. Butler, S. M. Hollen, L. Cao, Y. Cui, J. A. Gupta, H. R. Gutiérrez, T. F. Heinz, S. S. Hong, J. Huang, A. F. Ismach, E. Johnston-Halperin, M. Kuno, V. V. Plashnitsa, R. D. Robinson, R. S. Ruoff, S. Salahuddin, J. Shan, L. Shi, M. G. Spencer, M. Terrones, W. Windl and J. E. Goldberger, 2013, DOI: 10.1021/nn400280c.
- 4 A. Rasyotra, A. Thakur, B. Gaykwad, S. Chakrabarty, I. Bayad, J. Parikh and K. Jasuja, *J. Mater. Sci.*, 2023, **58**, 4359–4383.
- V. Shanmugam, R. A. Mensah, K. Babu, S. Gawusu, A. Chanda, Y. Tu, R. E. Neisiany, M. Försth, G. Sas and O. Das, *Part. Part. Syst. Charact.*, 2022, **39**, 2200031.
- 6 R. L. D. Whitby, ACS Nano, 2014, **8**, 9733–9754.
- 7 Z. Yuan, X. Xiao, J. Li, Z. Zhao, D. Yu and Q. Li, Adv. Sci., 2018, 5, 1700626.
- 8 S. Zhao, M. Li, X. Wu, S. H. Yu, W. Zhang, J. Luo, J. Wang, Y. Geng, Q. Gou and K. Sun, *Mater. Today Adv.*, 2020, **6**, 100060.
- 9 J. Hu, S. Zhang and B. Tang, *Energy Storage Mater.*, 2021, **34**, 260–281.
- S. Bera, M. Singh, R. Thantirige, S. K. Tiwary, B. T. Shook, E. Nieves, D. Raghavan, A. Karim and N. R. Pradhan, *Small Sci.*, 2023, **3**, 2300016.
- A. Qadir, T. K. Le, M. Malik, K. A. Amedome Min-Dianey, I. Saeed, Y. Yu, J. R. Choi, P. V Pham, S. K. Krishnan, E. Singh, P. Singh, M. Meyyappan and H. S. Nalwa, *RSC Adv.*, 2019, **9**, 23860–23880.
- 12 S. K. Krishnan, E. Singh, P. Singh, M. Meyyappan and H. S. Nalwa, RSC Adv., 2019,

View Article Online

DOI: 10.1039/D5NR01185J

- L. Ji, P. Meduri, V. Agubra, X. Xiao and M. Alcoutlabi, *Adv. Energy Mater.*, 2016, 6, 1502159.
- H. E. Karahan, K. Goh, C. (John) Zhang, E. Yang, C. Yıldırım, C. Y. Chuah, M. G. Ahunbay, J. Lee, Ş. B. Tantekin-Ersolmaz, Y. Chen and T.-H. Bae, *Adv. Mater.*, 2020, 32, 1906697.
- 15 X. Sun, C. Huang, L. Wang, L. Liang, Y. Cheng, W. Fei and Y. Li, *Adv. Mater.*, 2021,33, 2001105.
- M. G. Rasul, A. Kiziltas, B. Arfaei and R. Shahbazian-Yassar, *npj 2D Mater. Appl.*, 2021, **5**, 56.
- 17 H. Kim, A. A. Abdala and C. W. Macosko, *Macromolecules*, 2010, **43**, 6515–6530.
- 18 X. Wang, Y. Hu, L. Song, H. Yang, W. Xing and H. Lu, *J. Mater. Chem.*, 2011, **21**, 4222–4227.
- 19 W. Cai, X. Mu, Y. Pan, W. Guo, J. Wang, B. Yuan, X. Feng, Q. Tai and Y. Hu, *Polym. Adv. Technol.*, 2018, **29**, 2545–2552.
- 20 X. Wang, E. N. Kalali and D.-Y. Wang, J. Mater. Chem. A, 2015, 3, 24112–24120.
- 21 H. Riazi, S. K. Nemani, M. C. Grady, B. Anasori and M. Soroush, *J. Mater. Chem. A*, 2021, **9**, 8051–8098.
- 22 X. Sheng, Y. Zhao, L. Zhang and X. Lu, *Compos. Sci. Technol.*, 2019, **181**, 107710.
- S. Habibpour, K. Zarshenas, M. Zhang, M. Hamidinejad, L. Ma, C. B. Park and A. Yu, *ACS Appl. Mater. Interfaces*, 2022, **14**, 21521–21534.
- S. Chakrabarty, A. Thakur, A. Rasyotra, B. Gaykwad and K. Jasuja, *J. Phys. Chem. C*, 2023, 127, 852–870.
- 25 S. K. Das and K. Jasuja, ACS Appl. Nano Mater., 2018, 1, 1612–1622.
- 26 S. K. Das, A. Bedar, A. Kannan and K. Jasuja, *Sci. Rep.*, 2015, **5**, 10522.
- 27 A. L. James and K. Jasuja, *RSC Adv.*, 2017, 7, 1905–1914.
- A. Yousaf, M. S. Gilliam, S. L. Y. Chang, M. Augustin, Y. Guo, F. Tahir, M. Wang,

- A. Schwindt, X. S. Chu, D. O. Li, S. Kale, A. Debnath, Y. Liu, M. D. Green, E. J. Communication of the Continuous Santos, A. A. Green and Q. H. Wang, *J. Phys. Chem. C*, 2021, **125**, 6787–6799.
- A. Rasyotra, A. Thakur, S. Shukla, R. Mandalia, R. Ranganathan and K. Jasuja, *ACS Sustain. Chem. Eng.*, DOI:10.1021/acssuschemeng.4c06710.
- 30 B. Gaykwad, A. Thakur, A. Buch and K. Jasuja, *J. Phys. Chem. C*, DOI:10.1021/acs.jpcc.3c01388.
- A. Rasyotra, A. Thakur, R. Mandalia, R. Ranganathan and K. Jasuja, *Nanoscale*, 2023, **15**, 8204–8216.
- A. L. James, M. Lenka, N. Pandey, A. Ojha, A. Kumar, R. Saraswat, P. Thareja, V. Krishnan and K. Jasuja, *Nanoscale*, 2020, **12**, 17121–17131.
- 33 Z. Li, B. Zhao, L. Wang, Q. Tao and P. Zhu, *J. Phys. Condens. Matter*, 2023, **35**, 074002.
- 34 R. G. Munro, J. Res. Natl. Inst. Stand. Technol., 2000, 105, 709.
- E. Solfiti and F. Berto, *Procedia Struct. Integr.*, 2020, **25**, 420–429.
- 36 J. Xiao, L. Zhang, K. Zhou, J. Li, X. Xie and Z. Li, *Carbon N. Y.*, 2013, **65**, 53–62.
- 37 M. Wang, D. Chen, Z. Chen, Y. Wu, F. Wang, N. Ma and H. Wang, *Mater. Sci. Eng. A*, 2014, **590**, 246–254.
- M. Karbalaei Akbari, H. Baharvandi and K. Shirvanimoghaddam, *Mater. Des.*, DOI:10.1016/j.matdes.2014.10.048.
- 39 S. Venkatesan, J. Jerald, D. Sundeep, E. K. Varadharaj and C. C. Sastry, *Surf. Topogr. Metrol. Prop.*, 2022, **10**, 35003.
- 40 S. K. John and A. A. Anappara, New J. Chem., 2019, 43, 9953–9960.
- 41 R. Patidar, H. Gunda, A. K. Varma, R. Gawas, S. K. Das and K. Jasuja, *Ceram. Int.*, 2020, **46**, 28324–28331.
- F. M. de Souza, P. K. Kahol and R. K. Gupta, in *Polyurethane Chemistry: Renewable Polyols and Isocyanates*, American Chemical Society, 2021, vol. 1380, p. 1.
- 43 U. Khan, P. May, A. O'Neill and J. N. Coleman, *Carbon N. Y.*, 2010, **48**, 4035–4041.

- A. Pei, J.-M. Malho, J. Ruokolainen, Q. Zhou and L. A. Berglund, *Macromolecules*, 2011, 44, 4422–4427.
- 46 X. Dai, J. Xu, X. Guo, Y. Lu, D. Shen, N. Zhao, X. Luo and X. Zhang, *Macromolecules*, 2004, 37, 5615–5623.
- 47 S. L. Phua, L. Yang, C. L. Toh, S. Huang, Z. Tsakadze, S. K. Lau, Y.-W. Mai and X. Lu, ACS Appl. Mater. Interfaces, 2012, 4, 4571–4578.
- 48 S. Benli, Ü. Yilmazer, F. Pekel and S. Özkar, *J. Appl. Polym. Sci.*, 1998, **68**, 1057–1065.
- 49 P. A. Gunatillake, G. F. Meijs, S. J. Mccarthy and R. Adhikari, *J. Appl. Polym. Sci.*, 2000, **76**, 2026–2040.
- B. Fernández-d'Arlas, R. P. Baumann, E. Pöselt and A. J. Müller, *CrystEngComm*, 2017, **19**, 4720–4733.
- H. Zhang, L. Wang, Q. Chen, P. Li, A. Zhou, X. Cao and Q. Hu, *Mater. Des.*, 2016,92, 682–689.
- 52 Z. Li, M. Liu and R. J. Young, *Nano Mater. Sci.*, DOI:https://doi.org/10.1016/j.nanoms.2024.04.014.

Open Access Article. Published on 21 May 2025. Downloaded on 6/5/2025 2:17:29 PM.

- U. Khan, P. May, A. O'Neill, A. P. Bell, E. Boussac, A. Martin, J. Semple and J. N. Coleman, *Nanoscale*, 2013, **5**, 581–587.
- 54 M. Majdoub, Y. Essamlali, O. Amadine, I. Ganetri and M. Zahouily, *New J. Chem.*, 2019, **43**, 15659–15672.
- 55 S. Thakur and N. Karak, *RSC Adv.*, 2013, **3**, 9476–9482.
- C. Xiang, P. J. Cox, A. Kukovecz, B. Genorio, D. P. Hashim, Z. Yan, Z. Peng, C.-C. Hwang, G. Ruan, E. L. G. Samuel, P. M. Sudeep, Z. Konya, R. Vajtai, P. M. Ajayan and J. M. Tour, *ACS Nano*, 2013, 7, 10380–10386.
- 57 Y. Liu, N. Wu, S. Zheng, Y. Yang, B. Li, W. Liu, J. Liu and Z. Zeng, *ACS Appl. Mater. Interfaces*, 2022, **14**, 50120–50128.

Open Access Article. Published on 21 May 2025. Downloaded on 6/5/2025 2:17:29 PM.

View Article Online

- DOI: 10.1039/D5NR01185J
- 59 C. Cazan, A. Enesca and L. Andronic, *Polymers (Basel)*., DOI:10.3390/polym13122017.
- 60 N. Lempesis, P. J. in 't Veld and G. C. Rutledge, *Macromolecules*, 2017, **50**, 7399– 7409.
- 61 S. Zhu, N. Lempesis, P. J. in 't Veld and G. C. Rutledge, *Macromolecules*, 2018, 51, 1850-1864.
- 62 A. Talapatra and D. Datta, Mol. Simul., 2021, 47, 602–618.
- J. Koyanagi, N. Takase, K. Mori and T. Sakai, Compos. Part C Open Access, 2020, 2, 63 100041.
- 64 S. Mandal, D. Roy, K. Mukhopadhyay, M. Dwivedi and M. Joshi, RSC Appl. Interfaces, 2024, 1, 977–991.
- 65 A. Kumawat, K. Jasuja and C. Ghoroi, ACS Appl. Bio Mater., 2023, 6, 4111–4126.
- A. Niemczyk, A. Piegat, Á. Sonseca Olalla and M. El Fray, Eur. Polym. J., 2017, 93, 66 182-191.
- 67 A. K. Barick and D. K. Tripathy, *Mater. Sci. Eng. B*, 2011, **176**, 1435–1447.
- X. Li, H. Deng, Z. Li, H. Xiu, X. Qi, Q. Zhang, K. Wang, F. Chen and Q. Fu, Compos. 68 Part A Appl. Sci. Manuf., 2015, 68, 264-275.
- 69 R. J. Young, M. Liu, I. A. Kinloch, S. Li, X. Zhao, C. Vallés and D. G. Papageorgiou, Compos. Sci. Technol., 2018, 154, 110–116.
- 70 X. Lv, Z. Yin, Z. Yang, J. Chen, S. Zhang, S. Song and G. Yu, Recent Prog. Mater., 2024, **06**, 9.
- 71 C. Lee, X. Wei, J. W. Kysar and J. Hone, *Science* (80-.)., 2008, **321**, 385–388.
- 72 A. Jain, S. P. Ong, G. Hautier, W. Chen, W. D. Richards, S. Dacek, S. Cholia, D. Gunter, D. Skinner, G. Ceder and K. A. Persson, APL Mater., 2013, 1, 11002.
- 73 A. P. Thompson, H. M. Aktulga, R. Berger, D. S. Bolintineanu, W. M. Brown, P. S. Crozier, P. J. in 't Veld, A. Kohlmeyer, S. G. Moore, T. D. Nguyen, R. Shan, M. J. Stevens, J. Tranchida, C. Trott and S. J. Plimpton, Comput. Phys. Commun., 2022,

Nanoscale Accepted Manuscript

View Article Online DOI: 10.1039/D5NR01185J

271, 108171.

- 74 A. Stukowski, *Model. Simul. Mater. Sci. Eng.*, 2010, **18**, 15012.
- 75 S. Attarian and S. Xiao, *Comput. Mater. Sci.*, 2022, **201**, 110875.

Nanoscale Accepted Manuscript

View Article Online DOI: 10.1039/D5NR01185J

Data Availability

The data supporting this article have been included as part of the Electronic Supplementary File (ESI).